Acta Pharmaceutica Sinica B 2025;15(2):1143−1158

Chinese Pharmaceutical Association
Institute of Materia Medica, Chinese Academy of Medical Sciences

Acta Pharmaceutica Sinica B

www.elsevier.com/locate/apsb
www.sciencedirect.com

ORIGINAL ARTICLE

Modulating active targeting nanoparticle design according to tumor progressions

Huifang Nie, Rong Huang, Guangwei Jiang, Wenshuai Li, Lan Yang, Meng Zhang, Min Qian, Wei Guo, Tao Ye, Rongqin Huang*

School of Pharmacy, Key Laboratory of Smart Drug Delivery (Ministry of Education), Minhang Hospital, Fudan University, Shanghai 201203, China

Received 28 July 2024; received in revised form 25 September 2024; accepted 7 November 2024

KEY WORDS

Tumor progression;
Active targeting;
Particle size;
Tumor accumulation;
Receptor expression;
Pathophysiological characteristics

Abstract Targeting drug delivery systems mediated by nanoparticles has shown great potential in the diagnosis and treatment of cancer. However, influences of different tumor progressions on the accumulation of nanoparticles, especially the ligand-modified active targeting nanoparticles are seldom exploited. In this work, the accumulation and penetration of RGD-modified gold nanoparticles (active AuNPs) with different sizes were investigated in orthotopic breast cancer with different tumor progressions. The results showed that the smallest active AuNPs had better accumulation and permeation effects in early tumor tissues with the relatively looser extracellular matrix, larger gaps, lower interstitial fluid pressure, and less receptor expression, which was due to size effects. However, the larger active AuNPs had better accumulation and penetration effects in late tumor tissues with highly expressed target receptors integrin $\alpha_v\beta_3$ because of the multivalent interactions between larger active nanoparticles and integrin $\alpha_v\beta_3$. In the midterm, tumor accumulation of active AuNPs was equally influenced by size effects and multivalent interactions. Therefore, RGD-modified nanoparticles with sizes of 7 and 90 nm accumulated more in tumors. This study will guide a rational design of active targeting nanoparticles for enhancing the diagnosis and treatment of tumors based on their progressions.

*Corresponding author.
E-mail address: rqhuang@fudan.edu.cn (Rongqin Huang).

Peer review under the responsibility of Chinese Pharmaceutical Association and Institute of Materia Medica, Chinese Academy of Medical Sciences.

https://doi.org/10.1016/j.apsb.2024.12.016

1. Introduction

Nanoparticle-mediated targeting drug delivery has shown great potential in cancer diagnosis and treatment[1,2]. Thus, various nanoparticles with or without tumor-specific ligand modification have been widely developed for targeted delivery[3]. Even though, the drug delivery efficiency is still unsatisfactory due to poor retention of these nanocarriers within tumor[4-6]. At present, many researches focused on improving the physicochemical properties of nanoparticles, such as shapes, sizes, and surface chemistries, and developing various ligands including antibodies, peptides, or integrin ligands to enhance the tumor accumulation of nanoparticles[7-10]. Few studies have noticed the impact of the tumorous pathophysiological characteristics at different stages on the accumulation of targeted nanoparticles, especially the active targeting ones, in tumors. Factually, with the occurrence and development of tumors, the pathophysiological characteristics of tumor tissue change, which will lead to changes in the tumor accumulation efficiency of active targeting nanoparticles, and finally affect the drug delivery/therapeutic outcomes[11-13]. For instance, a great deal of studies has shown that extracellular matrix (ECM) can serve as a delivery barrier to prevent nanoparticles from entering tumor tissues, thereby affecting the targeted delivery effect of nanoparticles[11,12,14]. In addition, many studies have shown that the increased interstitial fluid pressure (IFP) in tumor tissues also hinders the entry of nanoparticles into their interior sites[15,16]. Moreover, with tumor progressions, the ECM of tumor cells becomes thicker and denser, and the interstitial fluid pressure also increases, thus producing a greater impact on the delivery effect of nanomedicines[17-19]. Therefore, investigation of the influence of pathophysiological changes in tumor tissues at different stages on tumor nanoparticle accumulation will give guidance to active targeting nanoparticle design, which is of great importance t for nano-drug developments.

Gold nanoparticles (AuNPs) have many advantages in nanomedical research such as high histocompatibility, adjustable particle sizes, easy realizations in targeted modification, and quantitative analysis[20,21]. RGD is a widely studied targeting peptide that is easy to modify onto the surface of gold nanoparticles[22-24]. Therefore, RGD-modified gold nanoparticles provided a facility to study the accumulation and permeability of active nanoparticles in tumor tissues at different progressions.

In this work, RGD-modified gold nanoparticles with four different sizes were prepared as active AuNPs and orthotopic breast cancer with different tumor progressions was used as the tumor model. Based on those, the accumulation and penetration effects of different active AuNPs in tumors with different progressions were investigated and compared (Fig. 1). When active nanoparticles enter the blood, they must first escape immune clearance and pass through the endothelium, then cross the tumor stroma layer to reach inside the tumor. Only the nanoparticles that arrive inside the tumor can be internalized by the tumor cells to achieve tumor diagnosis and treatment. Thus, we (i) analyzed the changes of pathophysiological characteristics in the progressions of the tumor, (ii) investigated the ability of active AuNPs with different sizes to be taken up by vascular endothelial cells and pass through blood vessels and tumor stroma, and (iii) discussed how changes in these pathophysiological characteristics involve permeation and retention of actively targeted AuNPs in the tumor. Understanding the relationship between tumor pathophysiological changes and tumor accumulation of active nanoparticles will enable clinicians to personalize cancer therapy by providing nanotherapeutic strategies according to tumor characteristics.

2. Materials and methods

2.1. Materials

HAuCl4·4H2O (≥99.7%) and hexadecyltrimethylammonium bromide (≥99.0%, CTAB) were derived from Sinopharm Chemical Reagent Co., Ltd. (Shanghai, China). L-Ascorbic acid (>99.0%), sodium borohydride (98%, $NaBH_4$), sodium citrate (98%, $C_6H_5O_7Na_3$), and colchicine were obtained from Aladdin (Shanghai, China). Filipin, phenylarsine oxide, and cell culture medium L-15 were purchased from Sigma (St. Louis, MO, USA). Meo-PEG-SH (Mw: 3500 Da) was bought from JenKem Technology Co., Ltd. (Beijing, China). RGD peptide was acquired from Sangon Biotech (Shanghai, China). NHS-PEG-SH (Mw: 3500 Da) and NH_2-PEG-SH (Mw: 3400 Da) were acquired from

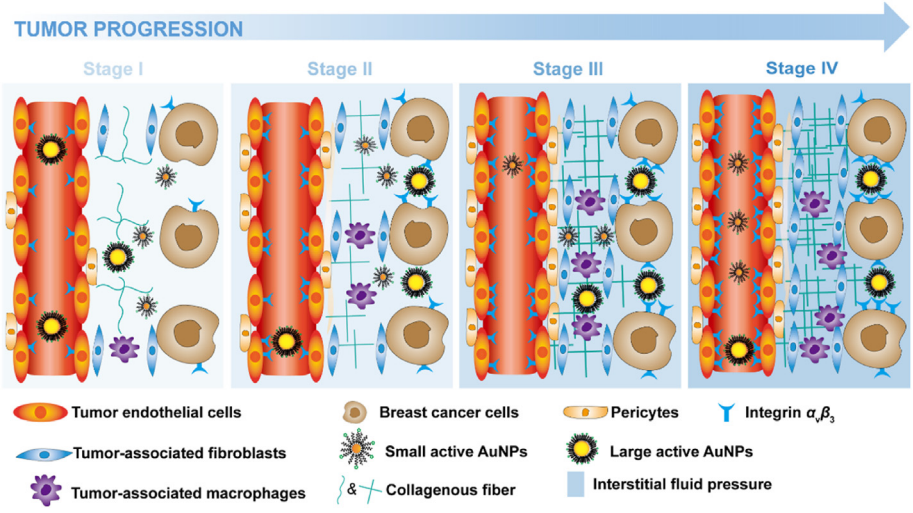

Figure 1 Schematic illustration of nanoparticles entering the blood circulation, passing through the blood vessel wall and tumor stroma, and entering the tumor tissues.

Ponsure Biotechnology (Shanghai, China). Cy5-NHS ester was bought from Duofluor Biotechnology (Wuhan, China). Aseptic grade PBS solution, DAPI, and Hoechst 33342 were obtained from Meilunbio Co., Ltd. (Dalian, China). Cell culture medium RPMI 1640, DMEM, Tyrisin, and penicillin−streptomycin were bought from Gibco (Tulsa, OK, USA). Fetal bovine serum (FBS) was obtained from Biochannel (Nanjing, China).

2.2. Synthesis and characterization of gold nanoparticles

The seed growth method was applied to synthesize 7-nm AuNPs as reported previously[25]. Firstly, the gold seeds (3.5 ± 0.7 nm) were acquired by reduction of $HAuCl_4 \cdot 4H_2O$. In brief, freshly acquired ice-cold NaBH4 solution (0.1 mol/L, 0.6 mL) was mixed with a mixture of $HAuCl_4 \cdot 4H_2O$ and sodium citrate aqueous solution (20 mL) with rapid stirring. After adding NaBH4, the aqueous solution turned pink instantaneously, indicating the formation of a particle. Secondly, the growth solution was obtained by CTAB (6 g) dissolved in $HAuCl_4 \cdot 4H_2O$ solution (0.25 mmol/L, 200 mL). Finally, seeding growth was applied to acquire the 7-nm AuNPs. Growth solution (15 mL) was mixed with L-ascorbic acid (0.1 mol/L, 0.1 mL) and then gold seeds solution (2.5 mL) was added under rapid stirring. The 15-nm AuNPs were prepared by standard reduction[26]. In brief, $HAuCl_4 \cdot 4H_2O$ solution (1% *w/v*, 1 mL) was added to deionized water (99 mL) and brought to a boil. Then, sodium citrate solution (1% *w/v*, 3 mL) was added to the boiling solution under vigorous stirring. After a complete color change, the solution continued to reflux for some time to obtain the 15-nm AuNPs. The synthesized 15-nm AuNPs also served as the seed solution for the synthesis of gold nanoparticles with a size of 45 nm. To prepare the 45-nm AuNPs, $HAuCl_4 \cdot 4H_2O$ solution (1% *w/v*, 997 μL) mixed with deionized water (96.7 mL) was hot to boiling and then 15-nm AuNP seeds (4.6 mL) were added into the boiling solution. Finally, sodium citrate solution (1% *w/v*, 1 mL) was mixed and stirred for 30 min. For the synthesis of 90-nm AuNPs, HAuCl4·4H2O solution (1% *w/v*, 550 μL) was mixed with deionized water (54.45 mL) and refluxed for 3 min. Under rapid Stirring, sodium citrate solution (1% *w/v*, 0.21 mL) was added to the solution and boiled for another 30 min.

The AuNPs with different sizes were fully characterized for morphology, size, zeta potentials, and UV−Vis absorbance. The homogenous morphology of AuNPs was observed by JEOL-2100F transmission electron microscopy (TEM; JEOL, Japan). The zeta potentials and size of AuNPs were detected with Malvern Zetasizer Nano ZS (Zetasizer Nano ZS ZEN3600, Malvern, Worcestershire, UK). UV−Vis absorbance was performed on a UV−Vis absorption spectrometer (2401 PC, SHIMADZU, Japan).

2.3. Surface modification of gold nanoparticles

The active AuNPs with different sizes were obtained as reported previously[8]. Firstly, PEG modification of RGD was obtained through the overnight reaction of cyclic RGD (fK) with NHS-PEG-SH (Mw: 3500 Da) at 4 °C in a PBS solution with a pH of 8.5. Then, the PEGylated RGD was mixed with MeO-PEG-SH (Mw: 3500 Da) at a 3:2 M ratio and modified onto gold nanoparticles by thiol chemistry. Finally, the RGD-modified AuNPs were separated from their supernatant by centrifugation. When the reaction of RGD modification of AuNPs was completed, the RGD in the supernatant and RGD standard solution with different concentrations were characterized by UV−Vis absorption spectrometer to calculate the density of RGD on the surface of AuNPs with different sizes. For the preparation of passive AuNPs, the AuNPs were modified with MeO-PEG-SH (Mw: 3500 Da) similar to the modification of active AuNPs. To visualize active or passive AuNPs, Cy5-NHS was reacted overnight with NH_2-PEG-SH (Mw: 3400 Da) at 4 °C in a PBS solution with a pH of 8.5. Then, the PEGylated RGD or MeO-PEG-SH was mixed with PEGylated Cy5 at a 3:2 M ratio and modified onto gold nanoparticles to obtain fluorescent labeling of active or passive AuNPs. The passive and active AuNPs were characterized with Malvern Zetasizer Nano ZS (Malvern), UV−Vis absorption spectrometer (SHIMADZU), Varian Mercury Plus-400 NMR spectrometer (Varian, USA), and FT-IR spectrometer (360FT-IR, Nicolet, USA). Fluorescence spectrums of fluorescently labeled AuNPs were obtained by Spectrofluorometer (Edinburgh FS5, UK).

2.4. Cell culture

All the cells were purchased from the Cell Bank of the Chinese Academy of Sciences (Shanghai, China) and grown at 37 °C in a humidified incubator with 5% CO_2. Human breast cancer (MDA-MB-231) cells were grown in an L-15 medium. Human mammary epithelial (MCF-10A) cells, human embryonic fibroblast (M 20) cells, and human umbilical vein endothelial (HUVEC) cells were incubated in a DMEM medium. Human peripheral blood monocytes (THP-1) were grown in the RPMI 1640 medium. All the growth media were supplemented with 10% FBS and 1% penicillin−streptomycin.

2.5. Cellular uptake of active AuNPs

HUVEC cells (1×10^6) were maintained in a 12-well plate and treated with Cy5-labeled active AuNPs at a dose equivalent to 14.12 cm^2/mL at 4 and 37 °C. After 3 h of treatment, the cells were digested for fluorescence intensity detection in flow cytometry (CytoFLEX S, Beckman, CA, USA). Cellular uptake of AuNPs was also executed in a confocal microscopy experiment. Cy5-labeled active AuNPs at a dose equivalent to 14.12 cm^2/mL were incubated with HUVEC for 3 h at 4 and 37 °C. Then, the cell nuclei were labeled with Hoechst 33342. Cy5-labeled active AuNP uptake in HUVEC cells was visualized by confocal microscope (LSM710, Carl Zeiss, Jena, Germany). Moreover, the cellular uptake efficiency of active AuNPs by HUVEC, MDA-MB-231, or MCF-10A cells was also determined by ICP-OES (ICP-8000DV03040404, PERKIN ELMER, Massachusetts, USA). In brief, cells were treated with active AuNPs at a dose equivalent to 14.12 cm^2/mL at 4 and 37 °C for 3 h. Then, the active AuNPs in HUVEC cells were digested in aqua regia and quantified by ICP-OES (PERKIN ELMER). The value of ICP-OES was normalized to the added dose to obtain the cellular uptake rate of active AuNPs.

2.6. The exploration of the endocytosis pathway of active AuNPs uptake by HUVECs

The endocytosis pathway of active AuNPs uptake by HUVECs was explored with CLSM and flow cytometry. For confocal microscope imaging, the cells were firstly cultured with free medium or medium containing colchicine (12, 24, 60 μg/mL), filipin (5, 10, 25 μg/mL), or phenylarsine oxide (PhAsO) (0.1, 0.25, 0.5 μg/mL) for 0.5 h. Then Cy5-labeled active AuNPs at a dose equivalent to 14.12 cm^2/mL were co-incubated with cells. After 3 h of treatment, Cy5-labeled AuNP signals generated from

HUVEC cells were examined by CSLM (Carl Zeiss). To quantify the above results, the cells were pretreated with free medium, colchicine (60 μg/mL), filipin (25 μg/mL), and phenylarsine oxide (PhAsO) (0.5 μg/mL) for 0.5 h. After incubating with Cy5-labeled active AuNPs at a dose equivalent to 14.12 cm^2/mL for 3 h, the internalized AuNPs were quantified using flow cytometry (Beckman).

2.7. The study of the ability of active AuNPs to cross vascular endothelial or fibroblast monolayers

Transwell assay was used to analyze the ability of active AuNPs to cross vascular endothelial or fibroblast monolayers. For the transendothelial ability, excess HUVEC cells were spread into the upper chamber of the Transwell membrane to form close conjugation. The Cy5-labeled active AuNPs were added to the upper chamber and treated at 4 and 37 °C for 2 h. The culture medium in the lower chamber was collected to determine the fluorescence intensity with a microplate reader (Synergy H1, BioTek, Vermont, USA) or CLSM (Carl Zeiss). The measured fluorescence intensity was normalized to the added fluorescence intensity in the upper chamber to obtain the accumulation transmembrane percentage. In addition, the 24-well Transwell plate containing the Cy5-labeled active AuNPs in the upper chamber was cocultured at 37 °C for 24 h to acquire accumulation transmembrane percentage of active AuNPs with different sizes within 24 h.

For the ability to cross fibroblast monolayers, excess M 20 cells were spread on the upper chamber of the Transwell membrane to form close conjugation. The Cy5-labeled active AuNPs were added to the upper chamber and cocultured at 37 °C. The culture medium in the lower chamber was collected at 2, 4, and 24 h later to determine the fluorescence intensity with a microplate reader (BioTek) or CLSM (Carl Zeiss).

2.8. Determination of the roles of integrin $\alpha_v\beta_3$ in cellular uptake

The role of integrin $\alpha_v\beta_3$ in cellular uptake was explored with CLSM and flow cytometry. In brief, MDA-MB-231cells were firstly pretreated with free RGD at concentrations of 0, 1, 5, and 10 μmol/L for 0.5 h and then treated with Cy5-labeled active AuNPs at a dose equivalent to 14.12 cm^2/mL for 3 h. Finally, the Cy5-labeled active AuNP signals in cells were examined by confocal microscopy (Carl Zeiss) and flow cytometry (Beckman).

2.9. Multicellular spheroid culture

MDA-MB-231 multicellular spheroids were implanted by the liquid overlay method as previously described. In brief, MDA-MB-231 cells (1×10^4) were implanted into 2% agarose attachment plates and cultivated for 7 days to form tumor spheroid.

For the formation of 3D coculture of MDA-MB-231 with M 20 cells, these two types of cells were firstly mixed in a 10:1, 5:1, 2:1, or 1:1 ratio, and then seeded into 2% agarose attachment plates and cultivated for 7 days to form multicellular spheroid.

To acquire a 3D coculture of MDA-MB-231 with THP-1 cells, MDA-MB-231 cells were plated into 2% agarose attachment plates at 1×10^4 cells/well. After 4 days of formation of tumor spheroids, THP-1 cells (1,000, 2,000, 5,000, or 10,000 cells/well) were added and allowed to coculture with tumor spheroids for an additional 4 days.

2.10. Permeation behavior of active AuNPs into multicellular spheroids

Cy5-labeled active or passive AuNPs were added into multicellular spheroids. After 24 h of treatment, the multicellular spheroids were then washed and fixed with 4% paraformaldehyde. The fixed multicellular spheroids were transferred to the 96-well plate for CLSM observations in Z-stacking scanning mode (Carl Zeiss).

2.11. Calculation of nanoparticle pharmacokinetics

A dose equivalent to 70.6 cm^2 of AuNPs was injected into the tail vein of SD rats. The blood was extracted at the designated time point (10 min, 0.5, 1, 2, 4,6, 8, 10, 12, 24, 48, and 72 h) and digested with aqua regia. The AuNP rate in blood was determined with ICP-OES (PERKIN ELMER). Clearance profiles were then fit to a one-compartment model as shown in Eq. (1) to compute the parameters presented in Table 2:

$$\mathrm{AuNP}_{\mathrm{plasma}}(t) = C_0 e^{-kt} \quad (1)$$

where C_0 and k denote the dosage for intravenous injection and stands for the first-order elimination rate constant, respectively.

2.12. Establishment of tumor models

To obtain *in-situ* breast cancer mouse models with different growth stages and volumes, the *in-situ* breast cancer mouse models were established by the time interval method. In brief, the tumor models at stage IV were established on Day 0, followed by stage III (on Day 7), and II (on Day 14) tumor models. The stage I tumor models were established on Day 21. The *in-situ* breast cancer mouse models were produced by subcutaneous implantation of 4×10^6 MDA-MB-231 cells into the fourth pair of breast pads on the left of 6-week-old female BALB/c nude mice. After the stage I tumors were established for 10 days, related experiments were carried out. All animal experiments were performed according to the guidelines evaluated and approved by the Ethics Committee of Fudan University (2021-03-YJ-HRQ-07).

2.13. The biodistribution, permeation, and accumulation behavior of active AuNPs in tumor

For the biodistribution and permeation behavior of active AuNPs in the tumor, a dose equivalent to 50 cm^2 of Cy5-labeled active AuNPs was intravenously administrated into mice *via* the lateral tail veins. The tumors were then collected from anesthetized mice and sliced into frozen sections 24 h later. The integrin $\alpha_v\beta_3$ and blood vessels were visualized *via* FITC-labeled anti-integrin alpha V beta 3 antibody (ab190147, Abcam) and anti-CD31 antibody (ab134168, Abcam), respectively. The biodistribution of active AuNPs in tumors was analyzed with CLSM and Bio-TEM observation.

To analyze the accumulation of active AuNPs in tumors, a dose equivalent to 50 cm^2 of Cy5-labeled active AuNPs was injected into the mice *via* the tail veins. All organs including the brain, heart, liver, spleen, lung, kidney, and tumor were collected from anesthetized mice 24 h later. The collected tissues were digested in aqua regia to quantify AuNP content in tissue by ICP-OES. AuNP accumulation rate in tissues was obtained by normalizing measured gold content to injection dose and tissue mass.

2.14. Tumor histology

After the stage I tumors reached about 100 mm^3 in volume, the tumors were collected from anesthetized mice. The collected tumors were then sectioned and stained with antibodies against integrin alpha V beta 3 (ab190147, Abcam), CD31 (ab134168, Abcam), α-SMA (17H19L35, Thermo Fisher Scientific), FAP (ab207178, Abcam), S100A4 (ab124805, Abcam), VEGF (ab234110, Abcam), LYVE-1 (ab219556, Abcam), CD68 (ab213363, Abcam), CD86 (ab239075, Abcam), CD163 (ab199427, Abcam) for confocal imaging. Picrosirius red-stained tumor sections were also used for collagen analysis.

2.15. Statistical analysis

The comparisons between data were executed by ANOVA. All graphics were prepared by using GraphPad Prism 9 and results were presented as means ± standard error of mean (SEM). $*P < 0.05$, $**P < 0.01$ and $***P < 0.001$.

3. Results and discussion

3.1. Nanoparticle design and characterizations

AuNPs with different diameters were first produced by seed growth method and standard reduction of gold (III) chloride trihydrate with sodium citrate, which exhibited uniform spherical morphology with sizes of 6.83 ± 0.63, 15.56 ± 1.09, 43.25 ± 5.20 and 91.43 ± 13.81 nm, respectively (Fig. 2A–D). The obvious lattice fringes with a spacing of 0.24 nm were observed for all these nanoparticles, indicating the high crystallinity of the as-prepared gold nanoparticles. The hydrodynamic diameters of different AuNPs as determined by dynamic light scattering (DLS)

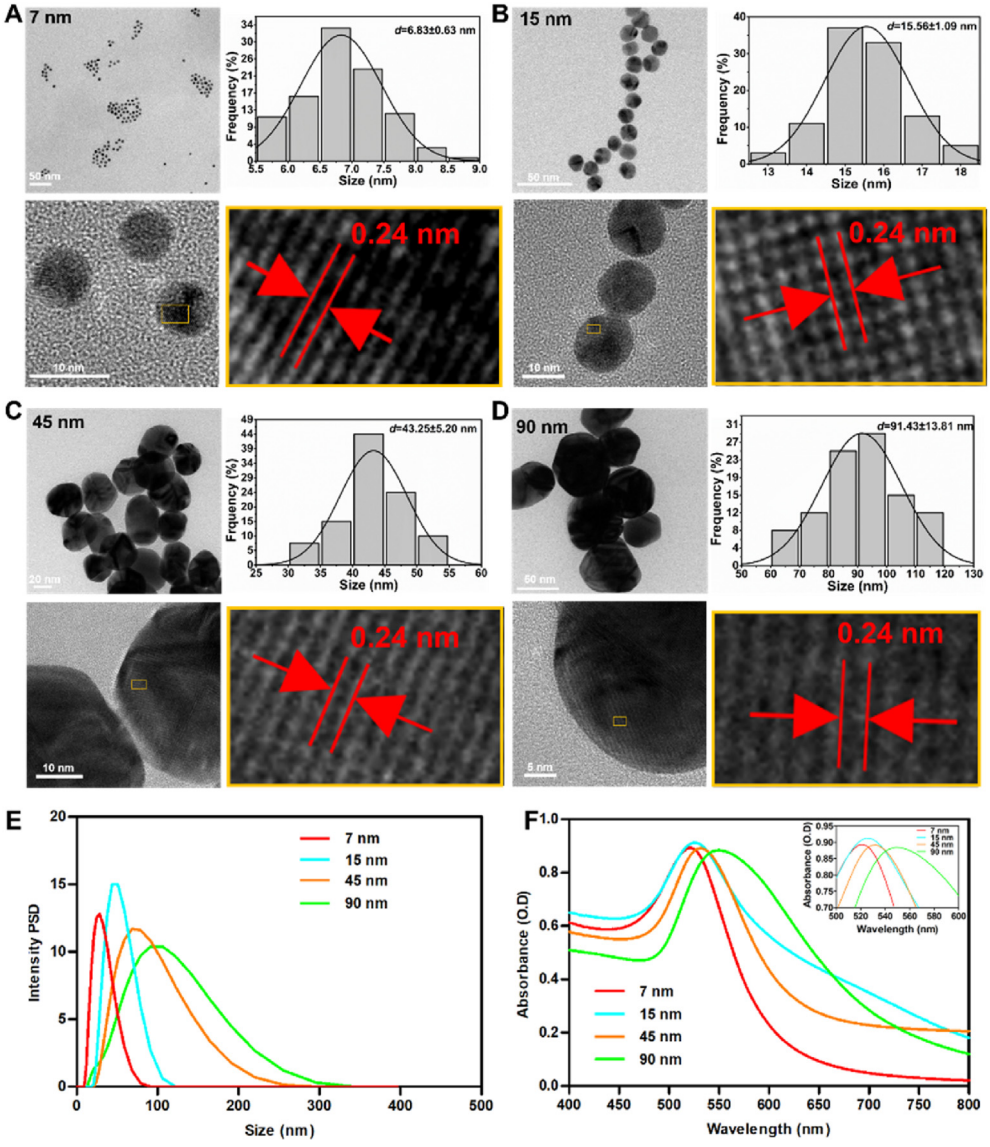

Figure 2 Nanoparticle synthesis and characterizations. (A–D) TEM images, corresponding histograms, and Gaussian fits of the measured AuNP size distribution as determined from their TEM micrographs, high-resolution TEM image, and locally enlarged image of AuNP with sizes 7 nm (A), 15 nm (B), 45 nm (C) and 90 nm (D). Hydrodynamic diameter distribution (E) and UV–Vis spectra (F) of different-sized AuNPs dispersed in water.

were only a little larger than their core diameters measured by TEM due to the hydration effect, suggesting their mono-dispersity (Fig. 2E). The z-potentials of as-synthesized AuNPs were also characterized and showed in Supporting Information Fig. S1. Since the 7-nm gold nanoparticle colloid was synthesized using hexadecyl methyl ammonium bromide (CTAB) as a stabilizer, its surface carried a positive charge. During the synthesis process, gold nanoparticle colloids of 15, 45, and 90 nm were stabilized with sodium citrate, resulting in negative charges on their surfaces. The formation of AuNPs with different sizes could also be validated by specific absorption peaks in the UV−Vis absorption spectra, which displayed a gradual red shift with the increased particle sizes (Fig. 2F). Then, the as-prepared AuNPs with different sizes were modified with PEG and RGD to form AuNPs with active targeting ability. The PEGylation and RGD modification were characterized by UV−Vis, ^{1}H NMR, and FT-IR spectra (Supporting Information Figs. S2A−S2C and S3A−S3C). The specific peaks labeled in the UV−vis, ^{1}H NMR, and FT-IR spectra showed that AuNPs were successfully modified with PEG and RGD. The density of RGD on the surface of AuNPs with different sizes was similar and about 0.1 RGDs/nm^2 (Supporting Information Fig. S4). To visualize gold nanoparticles in subsequent experiments, Cy5 fluorescence was modified on their surfaces (Supporting Information Fig. S5), which was validated by the fluorescence spectra. The hydrodynamic diameter and z-potentials of modified AuNPs were also characterized (Table 1). The modified AuNPs had similar negative z-potentials. Their hydrodynamic diameters were a little larger than those of pristine nanoparticles due to the polymer coating.

3.2. *Characterizations of pathophysiological changes in tumors with different progressions*

Pathophysiological changes of tumors with different progressions were analyzed to discern the biological parameters that might cause fluctuations in the targeting effect of active AuNPs. To simulate the progressions of tumors, the in-situ breast cancer mouse models established in female BALB/c nude mice were divided into four stages (I, II, III, and IV) according to the time of tumor establishment (Fig. 3A). The expression of targeted receptor integrin $\alpha_v\beta_3$ that might affect the targeting effect of RGD-modified AuNPs in different tumor progressions were firstly characterized by immunofluorescence staining of tumoral tissue section. The result indicated that the expression of integrin $\alpha_v\beta_3$ increased with the progression of tumors (Fig. 3B). Subsequently, the degree of vascularization was also characterized. The density of blood vessels visualized by CD31 antibodies staining was shown to increase with the progression of the tumor (Fig. 3C). Some studies have shown that the complex ECM components and collagen deposition form a compact fibrous barrier around tumor cells and contribute to solid stress and IFP, which greatly prevents the accumulation of nanoparticles in tumor tissues[27-30]. Therefore, collagen, one of the important components of ECM, was investigated *via* Picrosirius red staining and its polarized light. The imaging suggested that collagen gradually increased and deposited to form thick and straight collagen fibers in the progression of the tumor (Fig. 3D and E). Those collagen fibers formed an increasingly dense network and contributed to solid stress and IFP, which would prevent nanoparticles from entering the interior of the tumor and accumulating in the tumor. It is widely known that solid tumors consist of cancer cells and a large number of stromal cells such as fibroblasts, macrophages, etc. Tumor cancer-associated

Table 1 Characteristics of active and passive AuNPs.

AuNP	7-P	7-P/Cy5	7-P-R	7-P-R/Cy5	15-P	15-P/Cy5	15-P-R	15-P-R/Cy5	45-P	45-P/Cy5	45-P-R	45-P-R/Cy5	90-P	90-P/Cy5	90-P-R	90-P-R/Cy5
HD (nm)	23.1±0.8	25.3±0.5	28.8±1.6	29.2±0.9	41.3±0.1	42.5±0.1	42.1±0.9	40.8±0.1	52.5±0.1	58.1±2.1	55.0±1.7	53.5±1.0	97.4±1.8	94.1±0.6	94.0±2.6	93.5±0.8
Zeta potential (mV)	−17.1±2.8	−14.2±2.1	−16.9±0.7	−14.1±1.1	−18.7±1.2	−18.0±2.0	−16.7±1.0	−15.7±5.1	−21.6±2.9	−23.2±0.7	−20.2±0.5	−19.3±0.7	−22.7±0.6	−22.3±0.5	−21.7±0.4	−19.0±0.5

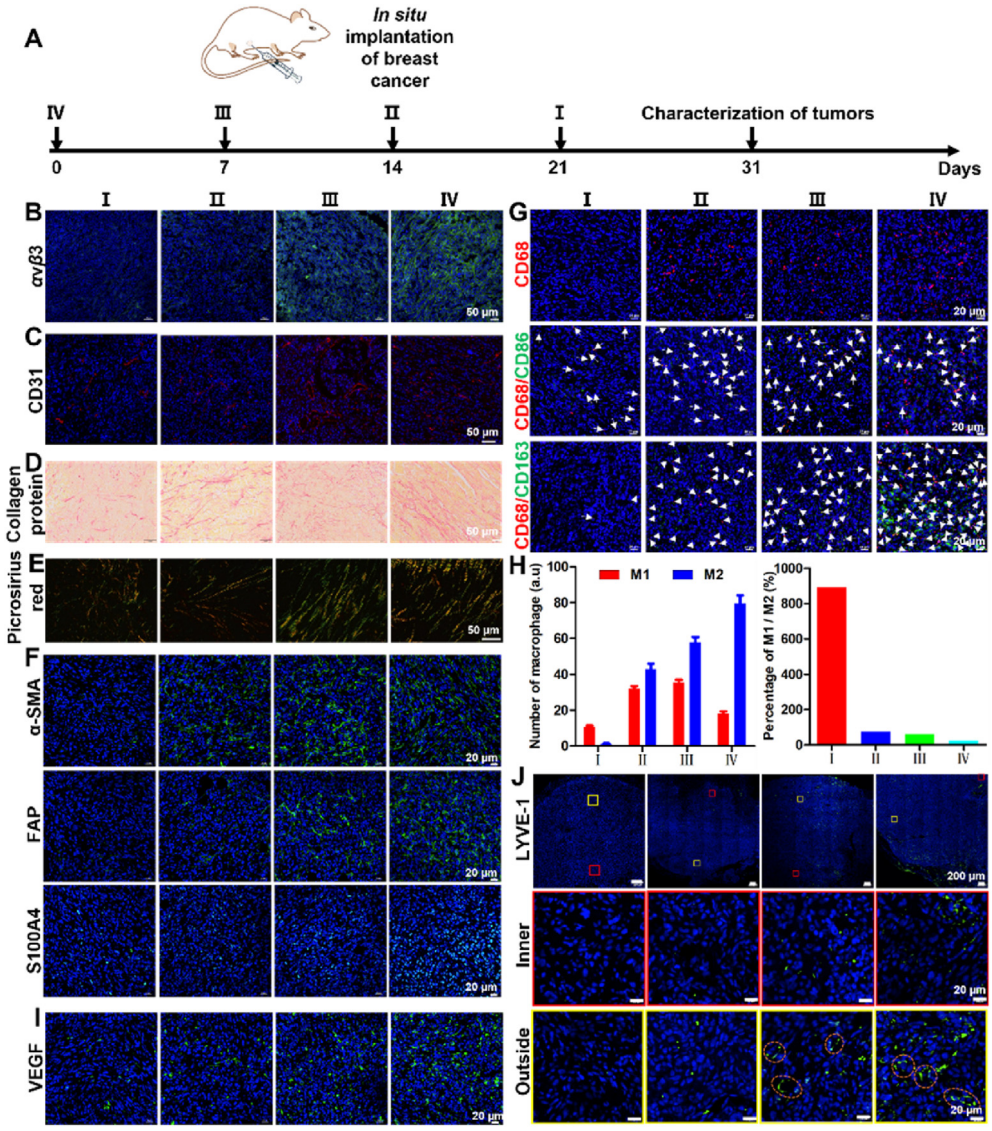

Figure 3 Physiological and pathological characterizations of tumor tissues during growth. (A) Schematic illustration of the establishment of the four stages of *in-situ* breast cancer mouse models by the time interval method. (B, C) Representative fluorescence images depicting the evolution of the expression of integrin $\alpha_v\beta_3$ (B) and vascular density (C) with tumor sizes. (D, E) Representative bright-field and polarized light images of sections stained with Picrosirius red describing the development of collagen with tumor sizes. (F) Immunofluorescence images of tumor section to analyze the expression of α-SMA, FAP, and S100A4 with tumor sizes. (G) Representative photographs of CD68/CD86/CD163 immunofluorescence staining depicting the change in the density of tumor-associated macrophages (CD68), M1 (CD68/CD86), and M2 (CD68/CD163) with tumor sizes. The white arrows indicate M1 or M2 cells. (H) Quantitative analysis of the amount of M1 and M2 macrophages in tumor tissues (left) and percentage of M1/M2 (right). (I) Representative photographs of VEGF immunofluorescence staining depicting the change of vascular permeability with tumor sizes. (J) Representative photographs of LYVE-1 immunofluorescence staining depicting the change of lymphatic permeability with tumor sizes. The yellow box is located at the edge of the tumor tissue, while the red box is located inside the tumor tissue. The lower panels are enlarged sections of the boxed regions from the upper panels. Dashed circles indicate lymphatic vessels. Data are mean ± SEM ($n = 10$).

fibroblasts (CAFs) are one of the most abundant tumor stromal cells and can secrete a large amount of ECM components such as collagen and fibronectin, increasing the density of the tumor matrix layer and preventing nanoparticles from entering tumor tissues[11,31,32]. Here, histological sections stained with α-SMA, FAP, and S100A4 antibodies were used to calorimetrically visualize CAFs. Confocal microscope images showed that CAFs increased with the progressions of the tumor (Fig. 3F). Studies have shown that cancer-associated macrophages can actively transport and redistribute nanoparticles in tumors after extravasation, and improve the depth of tumor penetration[33-35]. In addition, it is reported that the cellular uptake of nanoparticles by M2 macrophages is higher than that of M1 macrophages, and the ability of cellular uptake was positively related to the expression of CD163 on M2 macrophages[33,36]. In this study, tumor histological sections were stained with CD68/CD86/CD163 antibodies to observe macrophages and their subtypes (M1/M2). Confocal microscope images showed that the macrophages gradually increased and shifted from

M1 towards M2 with the progression of the tumor (Fig. 3G and H). Besides the changes in substantive factors, changes in other non-substantive factors such as IFP could also affect the entry of nanoparticles into tumor tissues. Numerous studies have shown that the presence of IFP in tumor tissues increases the entrance difficulty of drugs[12,37]. The numbers of fibroblasts and macrophages increased with the progression of the tumor proved as above, which could secrete growth factors and cytokines to act on vascular cells and stromal fibroblasts, resulting in increased IFP[37]. Moreover, the increase in vascular leakage led to the filtration of excess fluid from the blood vessels, thereby increasing the IFP within the tumor[27,37]. The permeability of blood vessels and lymphatic vessels was also analyzed by the expression of VEGF and LYVE-1. As shown in Fig. 3I, the expression of VEGF increased in the progression of the tumor, which indicated that the permeability of blood vessels was increased. The visualization of lymphatic vessels by immunofluorescence stained LYVE-1 in the tumoral tissue section showed that there were no complete lymphatic vessels inside the tumor tissues and only a few lymphatic vessels with normal structure appeared at the edges of the tumor tissues (Fig. 3J). The appearance of lymphatic vessels with normal structures at the edges of the tumor contributed to the metastasis of cancer cells during the progression. The absence or structural abnormality of lymphatic vessels within the tumors prevented the absorption and reflux of tissue fluid, resulting in high IFP.

To summarize, these results indicate that tumors undergo the increased expression of integrin $\alpha_v\beta_3$ and vascularization, where the vasculatures become denser and more chaotic as the tumor progresses. Particularly, when tumor fibrosis occurs, the ECM components such as collagen increase, deposit, thicken, and straighten during the progressions of the tumor, thus leading to a more amorphous and denser phenotype. Additionally, the number of stromal cells such as fibroblasts and macrophages increases, binding to increasingly dense ECM, leading to thickening and densification of the tumor stroma layer. The increased stromal cells secrete more cytokines and growth factors, coupled with increased vascular permeability and incomplete lymphatic vessels, resulting in an increased IFP in the progressions of the tumor.

3.3. Analysis of the ability of active AuNPs to cross vascular endothelial, tumor stromal and be internalized by tumor cells

After entering the bloodstream, nanoparticles are first internalized by vascular endothelial cells, then pass through the vascular wall and the tumor stroma layer. Finally, the nanoparticles in tumor tissue are absorbed by tumor cells to achieve diagnostic and therapeutic effects. In this study, the pharmacokinetics of functionalized AuNPs were analyzed by quantification of gold content in the blood of SD rats from 10 min to 72 h after tail vein injection. The result of ICP-OES revealed that the smaller active AuNPs had longer elimination half-life compared with larger active targeting AuNPs (Table 2). It has been reported that integrin $\alpha_v\beta_3$ is highly expressed on the surface of tumor vascular endothelial cells and tumor cells. HUVEC cells are often used as a research model for tumor vascular endothelial cells. The expression of integrin $\alpha_v\beta_3$ on HUVEC cells was analyzed by flow cytometry and confocal microscope, and proved to have high expression (Supporting Information Fig. S6). Subsequently, the ability of vascular endothelial cells to take up active AuNPs with different sizes was analyzed with flow cytometry and confocal visualization. As shown in Fig. 4B and C, Cy5-labeled active AuNPs with a core diameter around 90 nm (90-P-R/Cy5) had the best cellular uptake. A similar cellular uptake occurred on 7-nm (7-P-R/Cy5) and 45-nm (45-P-R/Cy5) active AuNPs. However, the active AuNPs with a core diameter around 15 nm (15-P-R/Cy5) had lower cellular uptake. A similar result was further validated by confocal microscopy imaging (Supporting Information Fig. S7). The result of cellular uptake of active AuNPs with different diameters may be caused by the size effect and multivalent interactions. The endocytosis of smaller nanoparticles required less energy compared with these larger nanoparticles, which makes the small-sized nanoparticles easy to be taken up by HUVEC cells. However, compared to smaller-sized nanoparticles, larger-sized RGD-modified AuNPs caused higher multivalent interactions with its target receptor integrin $\alpha_v\beta_3$ on the surface of HUVEC cells which facilitated their prompt internalization (Fig. 4A). The endocytosis mechanism was explored by flow cytometry and ICP-OES. The analysis of flow cytometry showed that a low temperature of 4 °C significantly limited the cellular uptake of active AuNPs as compared to 37 °C, demonstrating an energy-dependent endocytosis mechanism (Fig. 4D and Supporting Information Fig. S8A). The results of ICP-OES and confocal microscopy imaging once again confirmed this conclusion (Fig. 4E and Fig. S8B). Moreover, the analysis of ICP-OES also showed that the best cellular uptake rate occurred at 90-nm active AuNPs (90-P-R), which was consistent with the conclusion of fluorescence intensity analyzed by flow cytometry. This result also showed that energy changes had a greater effect on the internalization of large nanoparticles than that of small nanoparticles, which indicated that the endocytosis of small nanoparticles required less energy compared with that of large nanoparticles. To explore the internalization pathway of active AuNPs by HUVECs, the cells were pretreated with several endocytosis inhibitors. The cellular uptake of active AuNPs analyzed by flow cytometry was significantly reduced after HUVEC cells were pretreated with phenylarsine oxide (PhAsO), a clathrin-mediated endocytosis inhibitor, indicating the active gold nanoparticles were mainly internalized through clathrin-mediated endocytosis (Fig. 4F). After HUVEC cells pretreated with filipin, a caveolae-mediated endocytosis inhibitor, there was a decrease in relative fluorescence intensity especially in the internalization of larger nanoparticles, illustrating that the caveolae-mediated pathway was also partially involved in the internalization of active AuNPs. However, colchicine could not block the internalization of active gold nanoparticles, confirming that the active AuNPs were not internalized by the macropinocytosis pathway.

Table 2 Pharmacokinetic parameters of active and passive AuNPs.

AuNP	7-P-R	15-P-R	45-P-R	90-P-R	7-P	15-P	45-P	90-P
k (h^{-1})	0.0205	0.0259	0.0412	0.0631	0.0206	0.0193	0.0348	0.0643
$t_{1/2}$ (h)	33.81	27.76	17.26	11.82	40.21	35.87	21.30	11.04
C_0 (μg/mL)	6.35	16.66	39.15	84.23	7.83	11.57	33.34	82.86

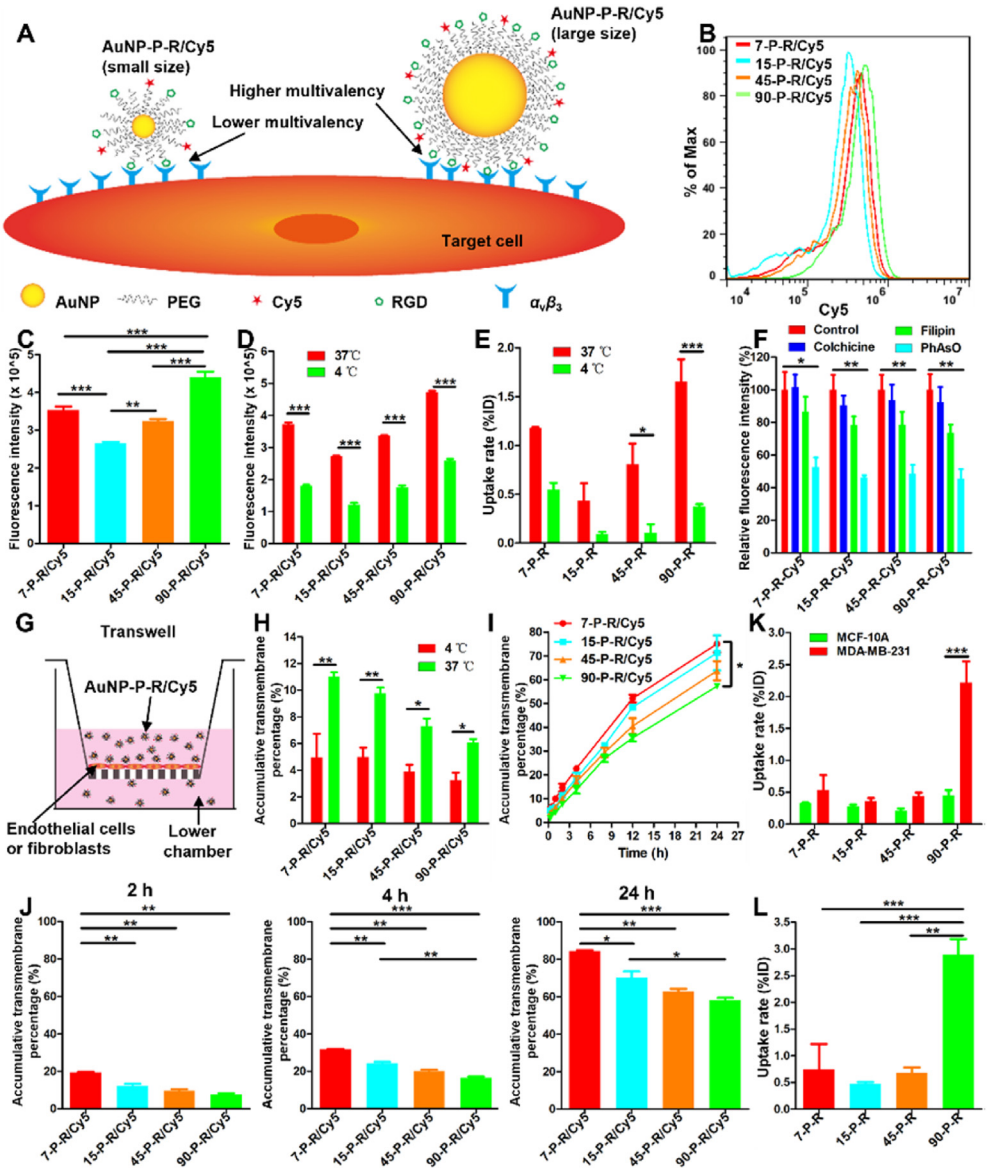

Figure 4 Analysis of the ability of nanoparticles to cross vascular endothelial HUVEC cell monolayers, fibroblast M 20 cell monolayers, and be taken up by tumor cells. (A) Diagrammatic sketch of the multivalent interactions between RGD and integrin $\alpha_v\beta_3$. (B, C) Flow cytometry analysis of endothelial cellular uptake of active AuNPs with different sizes. (D, E) Quantitative comparisons of endothelial cellular uptake of active AuNPs at 4 and 37 °C by flow cytometry (D) and ICP-OES (E). (F) Relative fluorescence intensity of active AuNPs taken up by endothelial cells incubated with endocytosis inhibitors such as colchicine, filipin, and PhAsO. Results were normalized to the fluorescence intensity of the control. (G) Schematic representations of the Transwell assay imitating the vascular wall or tumoral matrix barrier *in vitro*. (H) Transwell assay analysis of the ability of active AuNPs to cross vascular endothelial cells within 2 h at 4 and 37 °C. (I) Transwell assay analysis of the ability of active AuNPs to cross vascular endothelial cells within 24 h at 37 °C. (J) Transwell assay analysis of the ability of active AuNPs to pass through M 20 human embryonic fibroblast layers at 2, 4, and 24 h. (K) Recognition and uptake of active AuNPs by MCF-10A and MDA-MB-231 cells by ICP-OES. (L) ICP-OES analysis of MDA-MB-231 cellular uptake of active AuNPs with different sizes. Data are mean ± SEM. $*P < 0.05$; $**P < 0.01$; $***P < 0.001$; one-way ANOVA (C, I, J) and two-way ANOVA (D−F, H, K).

The confocal microscope images further confirmed that HUVEC cells internalized active AuNPs mainly through clathrin-mediated endocytosis, however, the caveolae-mediated pathway also partially involved the cellular uptake of larger formulations (Supporting Information Figs. S9 and S10). The way of nanoparticles across vascular endothelial cells is an active process which was demonstrated by the Transwell assay (Fig. 4G). At a low temperature of 4 °C, due to insufficient energy to support the transmembrane transport of nanoparticles, the accumulative transmembrane percentage of nanoparticles decreased significantly, which was also confirmed by confocal microscopy imaging of the liquid from the lower chamber (Fig. 4H and Supporting Information Fig. S11). The Transwell assay further showed that larger particles were more difficult to transport across the membrane compared with smaller particles at 24 h (Fig. 4I and Supporting Information Fig. S12). To enter the depth of tumor tissues, nanoparticles passing through the vascular wall are demanded further across the tumor matrix layer. The ability of

active nanoparticles to pass through the stromal cell layer was analyzed by the Transwell assay (Fig. 4G). The proportion of larger nanoparticles entering the lower chamber of the 24-well Transwell plate was significantly less than that of smaller nanoparticles, which was also confirmed by confocal microscopy imaging of the liquid from the lower chamber (Fig. 4J and Supporting Information Fig. S13). It indicates that nanoparticles with smaller sizes are easier to pass through the tumor matrix layer compared with larger nanoparticles. Only when nanoparticles are internalized by tumor cells can they achieve diagnosis and therapeutic effects. The expression of integrin $\alpha_v\beta_3$, a target receptor, on the normal breast cells (MCF-10A) and breast cancer cells (MDA-MB-231), was first analyzed by flow cytometry and confocal microscope. The results consistently indicated that human breast cancer cells have higher expression of integrin $\alpha_v\beta_3$ (Supporting Information Fig. S14). The ability of active nanoparticles to specifically distinguish between cancer cells and normal cells was explored by ICP-OES, flow cytometry, and confocal microscope. The results showed that RGD-modified AuNPs, especially the 90-nm active AuNPs among the four designed nanoparticles, could specifically recognize the MDA-MB-231 cells (Fig. 4K and Supporting Information Fig. S15). The 90-nm active AuNPs had the highest cellular uptake rate by MDA-MB-231 cells (Fig. 4L and Supporting Information Fig. S16). Those results can be explained by multivalent interactions as mentioned in HUVEC cellular uptake of the active AuNPs. The larger active particles had higher multivalent interactions *via* integrin $\alpha_v\beta_3$ expressed on MDA-MB-231 cells (Fig. 4A). Additionally, the analysis of flow cytometry and confocal microscope showed that the RGD modification could promote the internalization of nanoparticles, especially larger nanoparticles, by tumor cells (Supporting Information Fig. S17).

Together, the active AuNPs with smaller sizes had a longer elimination half-life in the blood and were more likely to penetrate the tumor stroma layer compared to active AuNPs with larger sizes. In addition, the way active AuNPs passed through vascular endothelial cells was an active transport process mediated by receptors and could specifically recognize tumor cells. Compared to larger-sized active AuNPs, although the amount of active AuNPs taken up by endothelial cells was lower, smaller-sized active AuNPs were more prone to exocytosis. Moreover, the largest (90-nm) and smallest (7-nm) sizes of active AuNPs were shown to have relatively high cellular uptake rates because of the multivalent interactions of large active AuNPs and the size effect of small active AuNPs.

3.4. Analysis of the effect of tumor stromal cells on penetration behavior of active nanoparticles in tumors using multicellular spheres

The effect of active targeting modification of nanoparticles on their tumor permeability was first analyzed by the multicellular spheres (MCSs) comprised of MDA-MB-231 cells. The confocal microscope imaging and quantitative analysis indicated that AuNPs modified with RGD had deeper penetration than passive AuNPs (Fig. 5A and B), which indicated that active targeting modification with RGD could enhance the permeability of nanoparticles. The influence of the size of active nanoparticles on their tumor permeability was also investigated with MCSs composed of MDA-MB-231 cells. The results showed that the smaller active AuNPs had higher penetration depth compared to larger active AuNPs (Fig. 5C and D). Due to the lack of IFP in MCSs, the penetration behavior of active nanoparticles is not affected by IFP. The nanoparticles with smaller sizes have strong tumor penetration ability and can easily escape the uptake of the outer layer of the tumor cells due to the weak multivalent binding effect. Nanoparticles entering the MCSs will remain inside the MCSs and will not be squeezed out, because there is no IFP inside the MCSs with a tiny volume. However, Due to the strong multivalent binding effect, large-sized nanoparticles are easily taken up by the tumor cells on the outer layer and fewer nanoparticles can escape the uptake of outer tumor cells to enter the interior of the tumor. The thick and hard tumor stroma plays an important role in inhibiting drug entry into the tumor interior. The CAFs are one of the most abundant tumor stromal cells and can secrete a large amount of ECM components to form a dense network to limit the drug's entry into the tumor interior. Thus, the model of 3D coculture of MDA-MB-231 with M 20 cells was used to observe the influence of CAFs on the penetration behavior of active AuNPs. The confocal microscope images and quantitative analysis confirmed that CAFs prevented the infiltration of nanoparticles into MCSs and had the largest inhibition on the permeability of large nanoparticles (Fig. 5E and F, and Supporting Information Fig. S18). Tumor-associated macrophages are abundant and exist in most tumors. It is well known that macrophages have a phagocytic function and can engulf foreign substances. Meanwhile, macrophages can infiltrate into the interior of the tissues. Therefore, the affection of macrophages on the infiltration of nanoparticles was analyzed with MCSs from 3D coculture of MDA-MB-231 with THP-1 cells. The results indicated that macrophages could promote nanoparticles penetrating MCSs (Fig. 5G and H, and Supporting Information Fig. S19). In a word, the increase of tumor fibroblasts is adverse to the entry of nanoparticles, especially large-sized active nanoparticles, into tumor tissues, while tumor-associated macrophages are favorable to the entry of nanoparticles into tumor tissues.

3.5. Analysis of nanoparticle accumulation, distribution, and penetration behavior into tumors

The active nanoparticle accumulation, distribution, and penetration in tumor tissues at different stages were evaluated on orthotopic breast cancer mouse models with different progressions (Fig. 6A). As shown by confocal microscopy imaging, the fluorescence intensity of the smallest active AuNPs (7-P-R/Cy5) distributed in tumor tissues reduced with the progression of tumor, and its best fluorescence intensity occurred in the stage I (Fig. 6B). On the contrary, the best fluorescence distribution of larger active AuNPs (15-P-R/Cy5 and 45-P-R/Cy5) occurred in the late tumor (stage IV). The fluorescence intensity of the largest active AuNPs (90-P-R/Cy5) distributed in tumor tissue increased first and then slightly decreased with the progression of the tumor. Moreover, in the early tumor (stage I), the fluorescence intensity of 7-P-R/Cy5 was significantly higher than the other three counterparts. To observe the influence of integrin $\alpha_v\beta_3$ expression on the distribution of RGD-modified nanoparticles in tumors, the target receptor integrin $\alpha_v\beta_3$ was manifested by immunofluorescence staining. With the development of tumor, the expression of integrin $\alpha_v\beta_3$ increased, and even with the increase of tumor interstitial fluid pressure and tumor stromal layer density, the biodistribution of larger active nanoparticles still increased, however, the distribution of 7-P-R/Cy5 decreased (Fig. 6C). The result revealed that the integrin $\alpha_v\beta_3$ highly expressed in tumor tissue had great influence on the accumulation of larger rather than

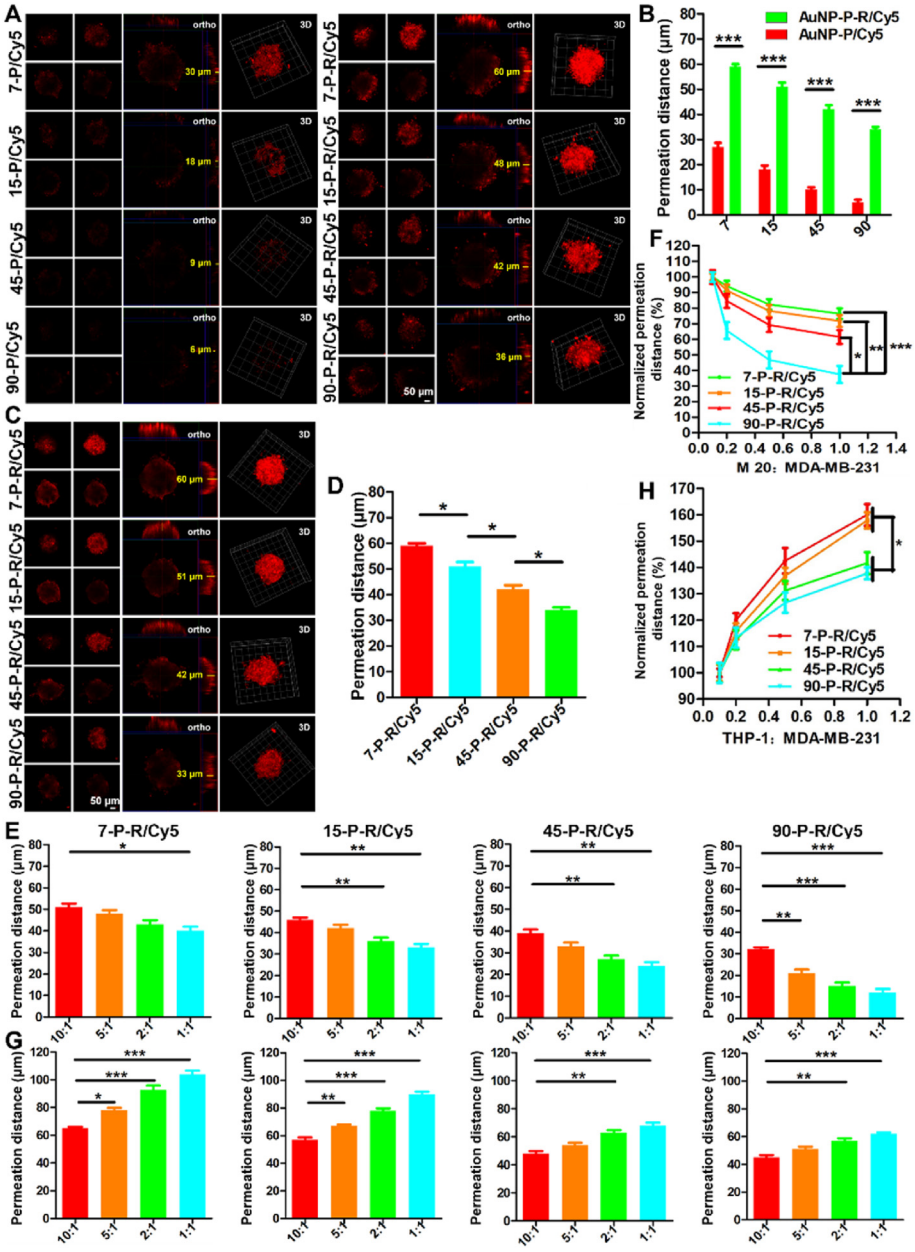

Figure 5 Permeation behavior of active AuNPs into tumor spheroids. (A) Representative confocal microscope images and (B) quantitative analysis of the pervasion distance of active and passive AuNPs into MDA-MB-231 tumor spheroids. (C) Representative confocal microscope images and (D) quantitative analysis of the pervasion distance of active AuNPs with different sizes into MDA-MB-231 tumor spheroids. (E) The analysis of the pervasion distance of active AuNPs with different sizes into 3D coculture of MDA-MB-231 with M 20 cells in a ratio of 10:1, 5:1, 2:1, and 1:1. (F) All the penetration distance in (E) was normalized to the mean of penetration distance in a ratio of 10:1. (G) The analysis of the penetration distance of active AuNPs with different sizes into 3D coculture of MDA-MB-231 with THP-1 cells in a ratio of 10:1, 5:1, 2:1, and 1:1. (H) All the penetration distance in (E) was normalized to the mean of penetration distance in a ratio of 10:1. Data are mean ± SEM ($n = 3$). $^{*}P < 0.05$; $^{**}P < 0.01$; $^{***}P < 0.001$; two-way ANOVA (B) and one-way ANOVA (D−H).

smaller active nanoparticles, which could be explained by multivalent interactions. The accumulation of active AuNPs was also quantified by ICP-OES. The smallest active AuNPs (7-P-R) had highest accumulation in the early tumor (stage I), while larger size nanoparticles (45-P-R and 90-P-R) had high accumulation in advanced and late tumor (stages III and IV) (Fig. 6D). The accumulation of the largest active AuNPs (90-P-R) in tumor tissues increased first and then slightly decreased with the development of tumor. The distribution and accumulation behavior of active particles could be explained by the pathophysiological changes in the progression of tumors and the size of nanoparticles. The pathophysiological changes associated with the development of tumors, such as vascular density, cell density, IFP, and the expression of integrin $\alpha_v\beta_3$. In the early tumor, the tumor tissues have a thinner tumor stroma layer with large gaps and lower IFP. The small-sized active nanoparticles have strong penetration ability and small resistance, so they can easily pass through the tumor matrix layer into the tumor interior. Few nanoparticles

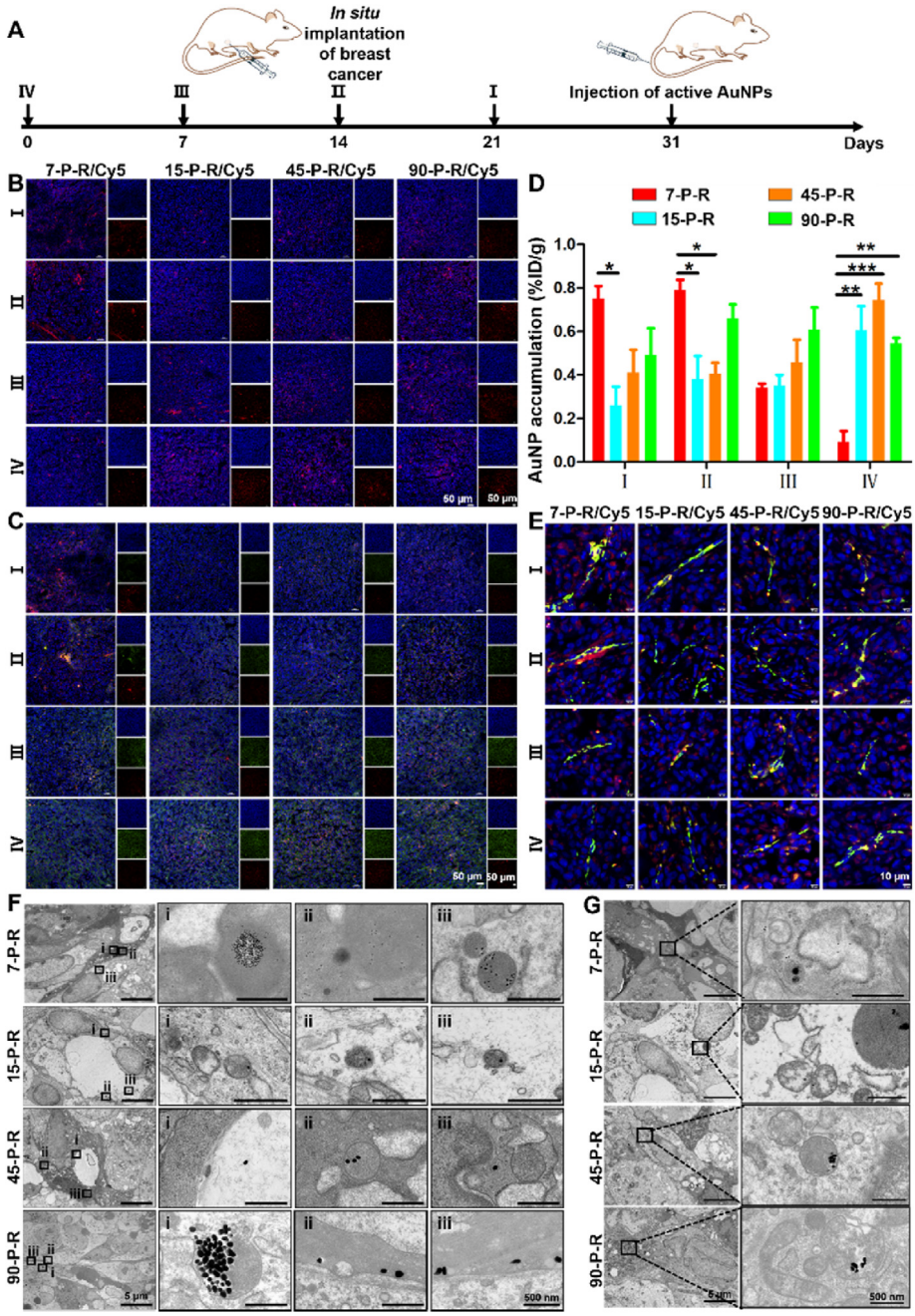

Figure 6 Accumulation and permeation of active AuNPs in tumor tissues. (A) Schematic illustration for evaluating the accumulation and permeation of active AuNPs on orthotopic breast cancer mouse models. (B) Fluorescence distribution of active AuNPs with different sizes in tumors of different volumes at 24 h after intravenous administration. (C) Fluorescence distribution of active AuNPs depicting how tumoral accumulation of AuNPs with different sizes varies with tumor volume and the expression of integrin $\alpha_v\beta_3$ at 24 h after intravenous administration. Red: Cy5-labeled active AuNPs; green: FITC-marked integrin $\alpha_v\beta_3$. (D) Quantitative analysis of active AuNPs levels in tumors with different volumes as measured by ICP-OES at 24 h after intravenous administration. Results were normalized to injection dose per gram of tumor. Data are mean ± SEM ($n = 3$). $^*P < 0.05$; $^{**}P < 0.01$; $^{***}P < 0.001$; two-way ANOVA. (E) Distribution of active AuNPs with different sizes away from tumor blood vessels at 24 h after intravenous administration. Red: Cy5-labeled active AuNPs; green: integrin $\alpha_v\beta_3$. (F, G) Representative TEM images of the transvascular (F) and tumor tissue permeability (G) of active AuNPs with different sizes in II tumors. Scale bars, 5 μm; insets, 500 nm.

entering tumor tissues will be squeezed out due to lower IFP. Therefore, the small active AuNPs (7-P-R) attained statistically higher accumulation in early tumor tissues. However, the lower vascular abundance and the expression of integrin $\alpha_v\beta_3$ in early tumor tissues are unfavorable to the transcapillary of larger active nanoparticles so that relatively few nanoparticles could cross blood vessels. In addition, larger particles have a weaker ability to penetrate the tumor matrix compared to small particles. Therefore, compared to small-sized active targeting nanoparticles, larger active nanoparticles had relatively less accumulation and

distribution in early tumor tissues. With the development of tumors, changes occur in the vascular density, ECM thickness, cell density, IFP, and the expression of integrin $\alpha_v\beta_3$ within the tumor tissues. The affluent blood vessels give nanoparticles more opportunities to enter tumor tissues. However, the increased cell density and collagen density make the tumor stroma thicker, denser, and harder, which increases the difficulty of nanoparticles passing through the stroma to enter tumor tissues. Increased IFP prevents nanoparticles from entering tumor tissues. The high expression of integrin $\alpha_v\beta_3$ increases the probability of cellular uptake of active particles, which is more beneficial for larger particles for multivalent interaction. Despite the poor ability of larger active nanoparticles to cross the tumor stroma, they will be promptly internalized by tumor cells once they arrive at the interior of tumor tissues and contact with tumor cells. The internalized active nanoparticles have less opportunity to be flushed out of tumor tissue again despite high IFP. However, even if the small active nanoparticles have a stronger ability to cross the tumor matrix, the nanoparticles that reach the interior of the tumor cannot be internalized quickly by the tumor cells and will be flushed out of the tumor tissues again by the high IFP. This phenomenon can be explained by the weaker multivalent interactions between small active nanoparticles with tumor cells. In summary, with the development of a tumor, changes in these pathophysiological factors, as well as the influence of the size of active nanoparticles, lead to a decrease in the tumor accumulation of small nanoparticles, while the tumor accumulation of larger nanoparticles increases. When tumors develop into late stages, the extracellular matrix layer is too dense and hard, which makes it difficult for nanoparticles with too large sizes to penetrate the tumor matrix layer and reach the interior of tumor tissues. Therefore, the accumulation of large active nanoparticles (90-P-R) was slightly reduced in the tumor at the late stage (stage IV). The accumulation of active nanoparticles in other organs was also analyzed by ICP-OES. The quantitative analysis results indicated that active AuNPs accumulated dominantly in the spleen and liver, only a small amount of which were distributed in other tissues such as the kidney, lung, and heart, and almost no nanoparticles entered into the brain (Supporting Information Fig. S20). It is presumed that the nanoparticles could easily enter the liver and spleen because of the abundant reticuloendothelial system (RES). The retention of nanoparticles in the tumor space is related to its proximity to blood vessels because particles near blood vessels are more likely to return to the bloodstream compared with deeper diffusing species. Thus, the penetration behavior of active AuNPs was explored by confocal microscopy imaging. As shown in Fig. 6E, the fluorescence intensity within a certain range around blood vessels was used to analyze the penetration depth. The smallest active AuNPs (7-P-R/Cy5) further diffused into the tumor microenvironment compared to larger sizes in early tumors (stage I) because of the strong permeability of smaller nanoparticles and lower IFP. The penetration depth of small active nanoparticles significantly decreased for the increased IFP with the development of tumors. Although larger active nanoparticles have poor permeability in early tumors for their size influence, their permeability will improve with the increase of vascular abundance and integrin $\alpha_v\beta_3$ expression in advanced and late tumors (stages III and IV). However, the ability of large nanoparticles (90-P-R/Cy5) to penetrate the tumor was weakened due to the thick and hard tumor matrix layer in the late stage (stage IV) and their large size. Furthermore, the penetration behavior of nanoparticles in stage II tumors was observed with bio-TEM. It was observed that a large number of active AuNPs with small (7-P-R) and large (90-P-R) sizes transported across the blood vessel wall (Fig. 6F), which could be explained by the strong permeability of small nanoparticles and excellent targeting ability of large nanoparticles. A lot of small and large nanoparticles were also found in distal tumor tissues (Fig. 6G).

In conclusion, the tumor accumulation and permeability of small-sized active nanoparticles decrease with the development of tumor tissues, which is due to the densification and hardening of tumor stroma and the increase in IFP. However, the tumor accumulation and permeability ability of large-sized active nanoparticles increases with the development of tumor tissues due to the increased multivalent binding effect. The accumulation and permeability of nanoparticles with too large sizes also decrease in late tumor tissues, as the dense tumor matrix layer of late tumor tissue prevents it from penetrating the interior of the tumor tissues. Therefore, active nanoparticles with small sizes have good accumulation and permeability in early tumor tissues, while those with larger sizes have good accumulation and permeability in late tumor tissues. In addition, the accumulation and permeability of nanoparticles with too large sizes also decrease in late tumor tissues.

3.6. A positive role of integrin $\alpha_v\beta_3$ in the tumoral accumulation of active nanoparticles

Some studies have shown that passive nanoparticles with larger sizes have little accumulation in tumors due to the poor penetrability of larger nanoparticles. In this study, larger active nanoparticles could also have higher tumor aggregation in advanced tumors than in early tumors. This may be caused by the high expression of integrin $\alpha_v\beta_3$ in advanced tumors, which produces stronger multivalent interactions between tumor cells and large nanoparticles. Therefore, the influence of the abundance of integrin $\alpha_v\beta_3$ on the internalization of nanoparticles by cells was analyzed with a confocal microscope and flow cytometry. After MDA-MB-231 cells were pretreated with RGD to block the number of integrin $\alpha_v\beta_3$, the cellular uptake of active AuNPs reduced significantly (Fig. 7A). Similar results were confirmed by flow cytometry (Fig. 7B and C). Further, colocalization of integrin $\alpha_v\beta_3$ with active nanoparticles in tumor tissues was analyzed by confocal microscopy imaging. The images and quantitative analysis of fluorescence intensity showed that active AuNPs were significantly aggregated in the place where integrin $\alpha_v\beta_3$ is highly expressed (Fig. 7D). In a word, the high expression of integrin $\alpha_v\beta_3$ has a positive influence on the cellular uptake and tumoral accumulation.

4. Conclusions

In this work, the accumulation and penetration of RGD-modified gold nanoparticles (active AuNPs) with different sizes were studied in the orthotopic breast cancer model with different tumor progressions. The results indicated that in early tumor tissues (stage I), the tumor stroma was relatively thinner, with larger gaps, lower IFP, and less receptor expression. The smallest active AuNPs (7-P-R) with strong permeability had better accumulation than the large counterparts (90-P-R) with poor permeability in the early tumor. In advanced tumors (stage III), the tumor stroma became dense, with smaller gaps, higher IFP, and higher receptor expression. Therefore, large-sized nanoparticles had a higher

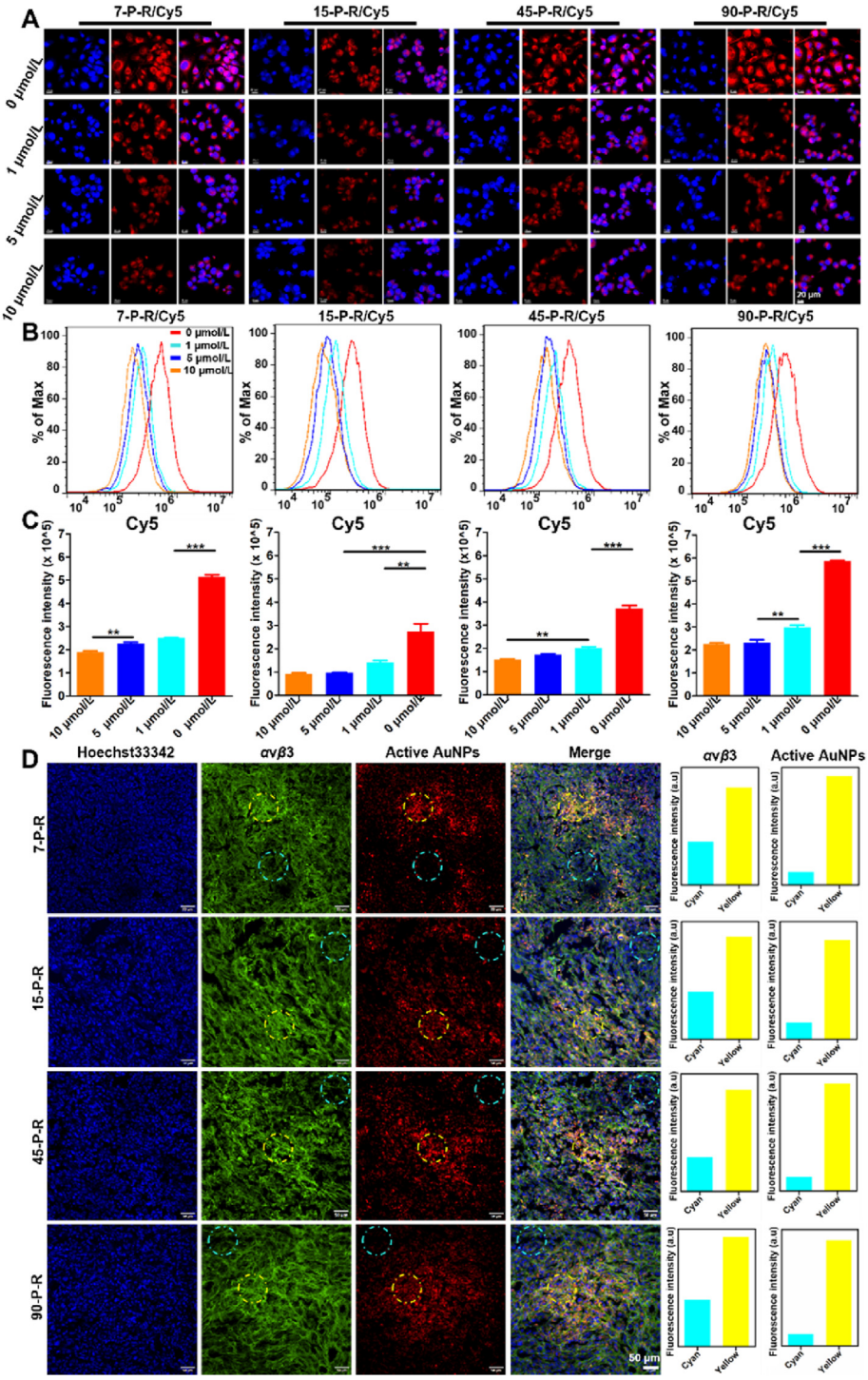

Figure 7 Effect of integrin $\alpha_v\beta_3$ expression on tumor cellular uptake and tumor tissue accumulation of active AuNPs. Confocal microscopy (A) and flow cytometric analysis (B) of the internalization of active AuNPs by MDA-MB-231 cells pretreated with RGD at concentrations of 1, 5, and 10 μmol/L. (C) Quantitative analysis of flow cytometric results. Data are mean ± SEM ($n = 3$). $^{**}P < 0.01$; $^{***}P < 0.001$; one-way ANOVA. (D) Confocal microscopy images of tumor tissue distribution of active AuNPs depicting the distribution of active AuNPs with the expression of integrin $\alpha_v\beta_3$ in the tumor. Right: quantitative analysis of fluorescence intensity of integrin $\alpha_v\beta_3$ and active AuNPs in cyan and yellow circles by Image J.

accumulation in advanced tumors due to their large surfaces mediated multivalent interactions between the highly expressed receptors in advanced tumors and the abundant RGD on the larger nanoparticles. However, the tumor accumulation of active nanoparticles with too large sizes was weakened by the thick and hard tumor matrix layer of the late tumor (stage IV). In the mid-term (stage II), tumor accumulation of active AuNPs was equally influenced by permeability and multivalent interactions.

Therefore, RGD-modified nanoparticles with sizes of 7 nm and 90 nm accumulated more in tumors. From the results of this study, we can recommend that actively targeted nanoparticles with small sizes should be selected as drug delivery systems for early cancer patients, however, the larger active nanoparticle can be chosen for designing drug delivery systems for advanced cancer patients. In a word, our results illustrated how the changes in pathophysiology characterizations with the tumor development influence the accumulation behavior of actively targeted nanoparticles, and provided recommendations for selecting appropriately sized active targeting delivery systems for cancer patients at different stages of development. Moreover, this conclusion is not only applicable to active spherical gold nanoparticles but also to other active spherical nanomaterials, such as other active spherical metal materials, active spherical silicon materials, etc. It can also be extended to other targeted molecules, such as transferrin, EGFR ligands, etc.

Acknowledgments

This work was supported by the Science and Technology Innovation Plan Laboratory Animal Research Project of Shanghai (23141900400), the National Natural Science Foundation of China (82172746 and 82473342), and International Cooperation Project of Shanghai Science and Technology Innovation Plan (24410741500). We thank Dr. Li Wang for performing the ICP experiments.

Author contributions

Huifang Nie: Writing − original draft, Validation, Project administration, Methodology, Investigation, Data curation, Conceptualization. Rong Huang: Methodology. Guangwei Jiang: Methodology. Wenshuai Li: Methodology. Lan Yang: Methodology. Meng Zhang: Methodology. Min Qian: Data curation. Wei Guo: Methodology. Tao Ye: Methodology. Rongqin Huang: Writing − review & editing, Validation, Supervision, Resources, Project administration, Methodology, Investigation, Funding acquisition, Data curation, Conceptualization.

Conflicts of interest

The authors declare no potential conflicts of interest.

Appendix A. Supporting information

Supporting information to this article can be found online at https://doi.org/10.1016/j.apsb.2024.12.016.

References

1. Yetisgin AA, Cetinel S, Zuvin M, Kosar A, Kutlu O. Therapeutic nanoparticles and their targeted delivery applications. *Molecules* 2020;**25**:2193.
2. Zhang W, Wang F, Hu C, Zhou Y, Gao H, Hu J. The progress and perspective of nanoparticle-enabled tumor metastasis treatment. *Acta Pharm Sin B* 2020;**10**:2037−53.
3. Dilliard SA, Siegwart DJ. Passive, active and endogenous organ-targeted lipid and polymer nanoparticles for delivery of genetic drugs. *Nat Rev Mater* 2023;**8**:282−300.
4. Shao Y, Xiang L, Zhang W, Chen Y. Responsive shape-shifting nanoarchitectonics and its application in tumor diagnosis and therapy. *J Control Release* 2022;**352**:600−18.
5. He Y, Fan X, Wu X, Hu T, Zhou F, Tan S, et al. pH-Responsive size-shrinkable mesoporous silica-based nanocarriers for improving tumor penetration and therapeutic efficacy. *Nanoscale* 2022;**14**:1271−84.
6. Hong Z, Sun X, Sun X, Cao J, Yang Z, Pan Z, et al. Enzyme-induced morphological transformation of drug carriers: implications for cytotoxicity and the retention time of antitumor agents. *Mater Sci Eng C Mater Biol Appl* 2021;**129**:112389.
7. Zhao Z, Ukidve A, Krishnan V, Mitragotri S. Effect of physicochemical and surface properties on *in vivo* fate of drug nanocarriers. *Adv Drug Deliv Rev* 2019;**143**:3−21.
8. Deng J, Wang J, Shi J, Li H, Lu M, Fan Z, et al. Tailoring the physicochemical properties of nanomaterials for immunomodulation. *Adv Drug Deliv Rev* 2022;**180**:114039.
9. Cong VT, Houng JL, Kavallaris M, Chen X, Tilley RD, Gooding JJ. How can we use the endocytosis pathways to design nanoparticle drug-delivery vehicles to target cancer cells over healthy cells?. *Chem Soc Rev* 2022;**51**:7531−59.
10. Wang Y, Wang J, Zhu D, Wang Y, Qing G, Zhang Y, et al. Effect of physicochemical properties on *in vivo* fate of nanoparticle-based cancer immunotherapies. *Acta Pharm Sin B* 2021;**11**:886−902.
11. Dai Y, Xu C, Sun X, Chen X. Nanoparticle design strategies for enhanced anticancer therapy by exploiting the tumour microenvironment. *Chem Soc Rev* 2017;**46**:3830−52.
12. Barua S, Mitragotri S. Challenges associated with penetration of nanoparticles across cell and tissue barriers: a review of current status and future prospects. *Nano Today* 2014;**9**:223−43.
13. Fang J, Islam W, Maeda H. Exploiting the dynamics of the EPR effect and strategies to improve the therapeutic effects of nanomedicines by using EPR effect enhancers. *Adv Drug Deliv Rev* 2020;**157**:142−60.
14. Zhao X, Chen R, Liu M, Feng J, Chen J, Hu K. Remodeling the blood-brain barrier microenvironment by natural products for brain tumor therapy. *Acta Pharm Sin B* 2017;**7**:541−53.
15. Gao Y, Shi Y, Fu M, Feng Y, Lin G, Kong D, et al. Simulation study of the effects of interstitial fluid pressure and blood flow velocity on transvascular transport of nanoparticles in tumor microenvironment. *Comput Methods Programs Biomed* 2020;**193**:105493.
16. Liu L, Kshirsagar PG, Gautam SK, Gulati M, Wafa EI, Christiansen JC, et al. Nanocarriers for pancreatic cancer imaging, treatments, and immunotherapies. *Theranostics* 2022;**12**:1030−60.
17. Hosein AN, Brekken RA, Maitra A. Pancreatic cancer stroma: an update on therapeutic targeting strategies. *Nat Rev Gastroenterol Hepatol* 2020;**17**:487−505.
18. Wang J, Han Y, Li Y, Zhang F, Cai M, Zhang X, et al. Targeting tumor physical microenvironment for improved radiotherapy. *Small Methods* 2022;**6**:e2200570.
19. Chen H, Zhang W, Zhu G, Xie J, Chen X. Rethinking cancer nanotheranostics. *Nat Rev Mater* 2017;**2**:17024.
20. Kesharwani P, Ma R, Sang L, Fatima M, Sheikh A, Abourehab MAS, et al. Gold nanoparticles and gold nanorods in the landscape of cancer therapy. *Mol Cancer* 2023;**22**:98.
21. Rai A, Seena S, Gagliardi T, Palma PJ. Advances in the design of amino acid and peptide synthesized gold nanoparticles for their applications. *Adv Colloid Interf Sci* 2023;**318**:102951.
22. Innocenti R, Dallari C, Lenci E, Pavone FS, Bianchini F, Credi C, et al. Design, synthesis and evaluation of RGD peptidomimetic−gold nanostar conjugates as M21 cell adhesion inhibitors. *Bioorg Chem* 2022;**126**:105873.
23. Liang G, Jin X, Zhang S, Xing D. RGD peptide-modified fluorescent gold nanoclusters as highly efficient tumor-targeted radiotherapy sensitizers. *Biomaterials* 2017;**144**:95−104.
24. Qin W, Chandra J, Abourehab MAS, Gupta N, Chen ZS, Kesharwani P, et al. New opportunities for RGD-engineered metal nanoparticles in cancer. *Mol Cancer* 2023;**22**:87.

25. Jana NR, Gearheart L, Murphy CJ. Seeding growth for size control of 5−40 nm diameter gold nanoparticles. *Langmuir* 2001;**17**:6782−6.
26. Liu Y, Wang Z, Liu Y, Zhu G, Jacobson O, Fu X, et al. Suppressing nanoparticle-mononuclear phagocyte system interactions of two-dimensional gold nanorings for improved tumor accumulation and photothermal ablation of tumors. *ACS Nano* 2017;**11**:10539−48.
27. Minchinton AI, Tannock IF. Drug penetration in solid tumours. *Nat Rev Cancer* 2006;**6**:583−92.
28. Stylianopoulos T, Munn LL, Jain RK. Reengineering the physical microenvironment of tumors to improve drug delivery and efficacy: from mathematical modeling to bench to bedside. *Trends Cancer* 2018;**4**:292−319.
29. Liu Y, Zhou J, Li Q, Li L, Jia Y, Geng F, et al. Tumor microenvironment remodeling-based penetration strategies to amplify nanodrug accessibility to tumor parenchyma. *Adv Drug Deliv Rev* 2021;**172**:80−103.
30. Zhang X, He C, Sun Y, Liu X, Chen Y, Chen C, et al. A smart O_2-generating nanocarrier optimizes drug transportation comprehensively for chemotherapy improving. *Acta Pharm Sin B* 2021;**11**:3608−21.
31. Chen X, Song E. Turning foes to friends: targeting cancer-associated fibroblasts. *Nat Rev Drug Discov* 2019;**18**:99−115.
32. Sahai E, Astsaturov I, Cukierman E, DeNardo DG, Egeblad M, Evans RM, et al. A framework for advancing our understanding of cancer-associated fibroblasts. *Nat Rev Cancer* 2020;**20**:174−86.
33. Ngambenjawong C, Gustafson HH, Pun SH. Progress in tumor-associated macrophage (TAM)-targeted therapeutics. *Adv Drug Deliv Rev* 2017;**114**:206−21.
34. Lin ZP, Nguyen LNM, Ouyang B, MacMillan P, Ngai J, Kingston BR, et al. Macrophages actively transport nanoparticles in tumors after extravasation. *ACS Nano* 2022;**16**:6080−92.
35. Nong J, Glassman PM, Myerson JW, Zuluaga-Ramirez V, Rodriguez-Garcia A, Mukalel A, et al. Targeted nanocarriers co-opting pulmonary intravascular leukocytes for drug delivery to the injured brain. *ACS Nano* 2023;**17**:13121−36.
36. MacParland SA, Tsoi KM, Ouyang B, Ma XZ, Manuel J, Fawaz A, et al. Phenotype determines nanoparticle uptake by human macrophages from liver and blood. *ACS Nano* 2017;**11**:2428−43.
37. Heldin CH, Rubin K, Pietras K, Ostman A. High interstitial fluid pressure—an obstacle in cancer therapy. *Nat Rev Cancer* 2004;**4**:806−13.